SCIENCE CHINA
Physics, Mechanics & Astronomy

•Article•

August 2021 Vol. 64 No. 8: 287311
https://doi.org/10.1007/s11433-020-1710-6

Measuring bulk and surface acoustic modes in diamond by angle-resolved Brillouin spectroscopy

YaRu Xie[1,2], ShuLiang Ren[1,2], YuanFei Gao[1,3], XueLu Liu[1,2], PingHeng Tan[1,2,3,4], and Jun Zhang[1,2,3,4*]

[1] *State Key Laboratory of Superlattices and Microstructures, Institute of Semiconductors, Chinese Academy of Sciences, Beijing 100083, China;*
[2] *Center of Materials Science and Optoelectronics Engineering, University of Chinese Academy of Sciences, Beijing 100049, China;*
[3] *Beijing Academy of Quantum Information Science, Beijing 100193, China;*
[4] *CAS Center of Excellence in Topological Quantum Computation, University of Chinese Academy of Sciences, Beijing 100049, China*

Received December 23, 2020; accepted April 30, 2021; published online July 1, 2021

The acoustic modes of diamond are not only of profound significance for studying its thermal conductivity, mechanical properties, and optical properties, but also play a definite role in the performance of high-frequency and high-power acoustic wave devices. Here, we report on the bulk acoustic waves (BAWs) and surface acoustic waves (SAWs) of single-crystal diamond using angle-resolved Brillouin light scattering (BLS) spectroscopy. We identify two high-speed surface skimming bulk waves (SSBW) with acoustic velocities of 1.277×10^6 and 1.727×10^6 cm/s, respectively. Furthermore, we obtain the relationship between the velocity of arbitrary BAWs and that of BAWs propagating along the high-symmetric axis at different incident angles. In the community of diamond-based acoustic studies, our results may provide a valuable reference for fundamental research and device engineering.

diamond, acoustic waves, angle-resolved Brillouin spectroscopy

PACS number(s): 77.65.Dq, 78.35.+c, 81.05.Uw, 43.20.Fn

Citation: Y. R. Xie, S. L. Ren, Y. F. Gao, X. L. Liu, P. H. Tan, and J. Zhang, Measuring bulk and surface acoustic modes in diamond by angle-resolved Brillouin spectroscopy, Sci. China-Phys. Mech. Astron. **64**, 287311 (2021), https://doi.org/10.1007/s11433-020-1710-6

1 Introduction

Bulk acoustic waves (BAWs) and surface acoustic waves (SAWs) are caused by density fluctuations in the matter and provide information about the elasticity, electrostriction, and thermal capacity of materials [1-3]. In communication and sensing devices, both SAW-based and BAW-based devices, such as acoustic radio frequency (RF) filters, resonators, and SAW microelectromechanical systems (MEMS), have been extensively applied [4-9]. The use of micro-acoustic devices considerably reduced the size of signal processors in the communications field. With the rapid development of mobile communications, additional high-frequency and high-power acoustic wave devices will be required [10].

Diamond shows excellent performance in high-frequency and high-power acoustic wave devices because of its superhigh elastic modulus and thermal conductivity, stable chemistry, and low thermal expansion coefficient and dielectric constant [11]. In high-frequency and high-power SAW devices, piezoelectric film/diamond multilayer structures have been extensively applied [12-14]. Furthermore, the emergent study of quantum acoustodynamics (QAD) cavities based on diamond contributes to the development of hybrid quantum devices [15,16]. The spins of single nega-

*Corresponding author (email: zhangjwill@semi.ac.cn)

tively charged Si vacancy (SiV) center [17,18] and nitrogen vacancy (NV) center [19,20] have a long coherence time, and these defects have achieved coherent interaction with SAWs. Therefore, additional research on the acoustic and physical properties of diamond is of great significance for designing high-performance acoustic wave devices.

Inelastic light scattering [21] is a precise method to detect phonons in solid materials. High-resolution Brillouin light scattering (BLS) spectroscopy is a noncontact, powerful method that has been extensively used to detect acoustic waves at frequencies of <300 GHz [3]. Two mechanisms contribute to the BLS process: scattering from BAWs through the elasto-optic mechanism, scattering from SAWs and SSBWs via the surface ripple [22]. In the past few decades, multiple different techniques, such as inelastic neutron scattering [23], inelastic synchrotron scattering [24], and ultrasonic pulse [25], have been used to investigate BAWs of solids. Compared with these techniques, BLS is more accurate and can measure acoustic signals at lower frequencies. Therefore, researchers prefer to use BLS to measure the acoustic properties of matter.

Prior research has used BLS to examine the BAWs of diamond. Grimsditch and Ramdas [26] measured BAWs along the high-symmetry direction of diamond and examined its elastic moduli and elasto-optic constants, but did not provide information of BAWs in other directions. Motochi et al. [27] obtained two SAW-like modes of chemical vapor deposition (CVD) diamond in BLS experiments; however, they did not explain the origins of these SAW-like modes. Therefore, it is necessary to explore angle-dependent properties of BAWs and investigate the physical mechanism of SAWs of diamond. Such a study should benefit the development of acoustic devices based on diamonds.

In this study, we report the angle-resolved BLS spectra of BAWs and SAWs of a diamond single-crystalline sample ((100) oriented) placed on a pristine Si wafer ((111) oriented). This study aims to explore the BAW frequencies of diamond dependent on the angle of incident light and explain the origins of two high-speed acoustic modes. With an increase in incident angle, the longitudinal acoustic (LA) peak shows a blueshift trend while the transverse acoustic (TA) peak gradually splits into two branches. We attribute this phenomenon to the velocity diversity of the acoustic mode along different crystal directions. Furthermore, we identify three modes propagating along the surface: Rayleigh SAW (RSAW), surface skimming transverse wave (SSTW), and surface skimming longitudinal wave (SSLW) whose velocities are 1.080×10^6, 1.277×10^6, and 1.727×10^6 cm/s, respectively.

2 Experimental details

Figure 1 shows our experimental setup, and we use a confocal microscope system to measure the BLS spectra of diamond in the backscattering geometry. The system is composed of high contrast (~10^{15}) (3+3)-pass tandem Fabry-Pérot interferometers (FPI) and a confocal microscope (CM) with a 20× bright field objective lens (numerical aperture NA=0.42) both from JRS Scientific Instruments in Switzerland. The detector is a Hamamatsu H10682-110 with a quantum efficiency of 10.8%. When the laser passes through the polarizing beam splitter (PBS), the *s*-polarized light is almost totally reflected to reach the sample while the *p*-polarized component is nearly completely transmitted. The incident light is emitted from a single longitudinal mode laser source at 532 nm and focused on the top surface of the diamond. The confocal setup assures that the collected scattering information is from as near to the surface as possible. Although the laser power is 29 mW, we did not observe any laser heating effect on the sample owing to the high thermal conductivity of diamond. In our experiments, there are three polarization configurations: circular polarization ($\sigma^+\sigma^-$), parallel polarization (VV), and cross polarization (VH). The three polarizations correspond to only the quarter wave plate (QWP) in the light path, both the QWP and polarizer in the light path, as well as neither the QWP nor polarizer in the light path. Here, the first and second items of polarization abbreviation describe the polarization of the incident and scattered light, respectively. In particular, σ^+ (σ^-), V, and H represent right (left) circular polarization, *s*-polarization, and *p*-polarization, respectively.

A 3 mm×3 mm×0.25 mm diamond, purchased from Element Six Technologies of the Anglo American PLC, is a type IIa single crystal synthesized by CVD. It has extremely low dislocation density and defect concentration, where the boron concentration is <0.05 ppm and the nitrogen con-

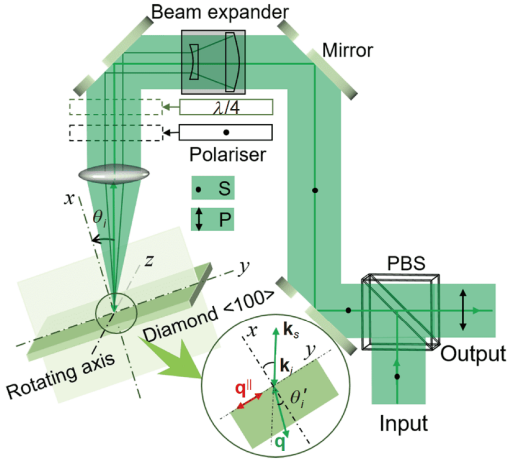

Figure 1 (Color online) Experimental setup. Only the *s*-polarized component of incident light is completely reflected by the PBS and finally focuses on the diamond surface. The inset is a schematic diagram of light and phonon wave vectors on the *x*-*o*-*y* plane, where phonons include SAW (wave vector is $\mathbf{q}^{\parallel}$) and BAW (wave vector is $\mathbf{q}$). θ'_i is the refraction angle inside the diamond.

centration is <1 ppm. There are two (100) oriented surfaces that are polished with a roughness <30 nm and the 12 edges are along the <100> orientation with miscuts within 3°. The diamond is placed on a Si wafer and then fixed on a home-built angle-resolved holder that can be rotated around the *z*-axis, as shown in Figure 1. The incident angle θ_i is adjusted by rotating the diamond to achieve angle-resolved BLS measurements. The rotation accuracy is <1°. The parameters of the diamond are density ρ=3.515 g/cm^3 and refractive index n=2.426 when λ=532 nm.

3 Results and discussion

BLS is an inelastic scattering of light from acoustic phonons because of the density fluctuations of materials [28,29]. In the Brillouin shift, the frequency f of a scattered acoustic wave is written as follows:

$$f = qv, \tag{1}$$

where $v = \sqrt{X/\rho}$ is the acoustic velocity; X is an expression composed of the elastic modulus C_{ij}; ρ is the density of sample; and q is the magnitude of wave vector **q**.

For a given wave vector of incident light $\mathbf{k}_i$ under back-scattering geometry, the detected BAW wave vector is $\mathbf{q}=\pm 2n\mathbf{k}_i$ and the SAW wave vector is $\mathbf{q}^{\parallel}=\pm 2\mathbf{k}_i\sin\theta_i$ where θ_i is the incident angle [30]. Therefore, both **q** and $\mathbf{q}^{\parallel}$ are equal to $\pm 5.73\times 10^5$ cm^{-1} and $\pm 2.36\sin\theta_i\times 10^5$ cm^{-1} in our BLS experiments, respectively, i.e., the BAW wave vector in the sample is a constant, while the SAW wave vector is proportional to $\sin\theta_i$. Because of the nonnegligible numerical aperture of the objective lens, $\mathbf{q}^{\parallel}$ has an angle-dependent uncertainty $\Delta q^{\parallel}$. Under the given conditions, the magnitude of $\Delta q^{\parallel}$ is $\Delta q^{\parallel}=2k_i\cos\theta_i\times NA$, where NA is the numerical aperture of the objective lens. Therefore, the spectra of SAW broadened at a smaller θ_i. The NA of our objective lens is 0.42, such that the SAW $\Delta q^{\parallel}$ is ~1×10^5 cm^{-1} under normal incidence. With θ_i approaching 90°, the full width at half maximum (FWHM) of SAW decreases. Selecting an appropriate objective lens can effectively suppress such a broadening effect.

For an arbitrary propagation direction, there are two quasi-TA modes and one quasi-LA mode. Usually, LA mode propagates faster than the TA mode [3]. We list the acoustic velocities of diamond previously reported [24,25] and our measured velocities in Table 1. In the BLS spectra, the intensity and polarization properties of scattering signals are determined by the scattering tensors of the acoustic modes. Scattering tensors are dependent on the direction of wave vector **q** of the scattered acoustic phonons. For **q** parallel to the [100] orientation, the scattering tensors **T** of BAWs along three different vibration directions are listed below:

$$\text{LA: } \mathbf{u}=[100],\ \mathbf{T}=\varepsilon_0^2\begin{bmatrix} p_{11} & 0 & 0 \\ 0 & p_{12} & 0 \\ 0 & 0 & p_{12} \end{bmatrix}, \tag{2}$$

$$\text{TA}_1\text{: } \mathbf{u}=[001],\ \mathbf{T}=\varepsilon_0^2\begin{bmatrix} 0 & 0 & p_{44} \\ 0 & 0 & 0 \\ p_{44} & 0 & 0 \end{bmatrix}, \tag{3}$$

$$\text{TA}_2\text{: } \mathbf{u}=[010],\ \mathbf{T}=\varepsilon_0^2\begin{bmatrix} 0 & p_{44} & 0 \\ p_{44} & 0 & 0 \\ 0 & 0 & 0 \end{bmatrix}, \tag{4}$$

where **u** is the vibration direction of phonons traveling along **q**, ε_0 is the dielectric constant of the material, and p_{ij} is the elasto-optic constant. Under a given polarization configuration, the intensity I of a scattered peak is proportional to $[\hat{e}_s\cdot\mathrm{T}\cdot\hat{e}_i]^2$, where $\hat{e}_s$ and $\hat{e}_i$ are unit vectors along the polarization direction of the scattered and incident light, respectively. Under VV polarization, the $[\hat{e}_s\cdot\mathrm{T}\cdot\hat{e}_i]^2$ of the LA mode is proportional to p_{12}^2 while both TA modes are undetectable; under VH polarization, only the $[\hat{e}_s\cdot\mathrm{T}\cdot\hat{e}_i]^2$ of

Table 1 Acoustic velocity of diamond

Propagation direction of **q**	Velocity of acoustic mode	Previous reports (×10^6 cm/s)	This work (×10^6 cm/s)	Vibration direction of mode
100 (Γ-X)	v_{LA}	1.751[a)]	1.744±0.0005	010/001
	v_{TA}	1.282[a)]	1.268±0.0001	100
110 (Γ-K)	v_{LA}	1.833[b)]	1.822±0.0042	110
	v_{TA1}	1.282[b)]	1.268±0.0003	001
	v_{TA2}	1.166[b)]	1.173±0.0001	$1\bar{1}0$
111 (Γ-L)	v_{LA}	1.857[a)]	–	111
	v_{TA}	1.208[a)]	–	$1\bar{1}0/11\bar{2}$
100 → 110 (Γ-A)	v_{LA}	–	1.744-1.784	–
	v_{TA}		1.268-1.218	

a) Calculated by $v_{LA}=\sqrt{C_{11}/\rho}$ and $v_{TA}=\sqrt{C_{44}/\rho}$ where ρ=3.512 g/cm^3 is the density of diamond in this study. The elastic moduli C_{44} and C_{11} are cited from ref. [25].

b) Ref. [24].

the TA_1 mode is not zero; and for $\sigma^+\sigma^-$ polarization, all modes can be measured.

Figure 2(a)-(c) show the angle-resolved BLS spectra of diamond under three polarization configurations. The LA mode is undetectable in VH polarization and the TA mode is not detected in VV polarization. When the laser is perpendicularly incident on the sample surface (i.e., θ_i=0), the measured frequencies of LA and TA modes are ~159 and ~116 GHz, respectively. Based on the measured frequency, we report that their velocities are consistent with LA and TA modes along the Γ-X direction [25]. With increasing θ_i, the frequency of the LA mode has a blueshift, and the TA mode gradually splits into two peaks: one with an unchanged frequency at 116 GHz and the other with a redshift, as shown in Figure 2(d)-(g). Gradually, the A, B, and C modes appear on the spectra with increasing θ_i and their frequencies are possibly proportional to θ_i, as shown in Figure 2(h). In Figure 2(i), A and B modes are close together and almost merge into one broad peak, which has a VH polarization. Here, we only show the spectra of A and B modes under VH polarization because spurious signals affect the analysis of peaks in the 30-40 GHz range for both VV and $\sigma^+\sigma^-$ configurations.

Figure 3(a) shows the 1/8 zone of the first Brillouin zone (BZ) of the diamond [31]. Because the point group of the diamond belongs to O_h with 48 symmetry elements: the first BZ can be divided into 48 equivalent irreducible wedges (IWs) [32]. The IWs are shown as the shaded area in Figure 3(a) and bounded by the three high symmetry axes, Γ-X, Γ-K, and Γ-L. Each IW contains all BAWs in the diamond. As per our experimental geometry, the wave vectors of incident light and scattering light vary in the *x*-*o*-*y* plane of the IW. As shown in Figure 3(b), the measured BAWs propagate along or against the direction of refracted light (Γ-A direction) with a velocity of $\mathbf{v}_{\Gamma A}$. Therefore, the wave vector of scattered

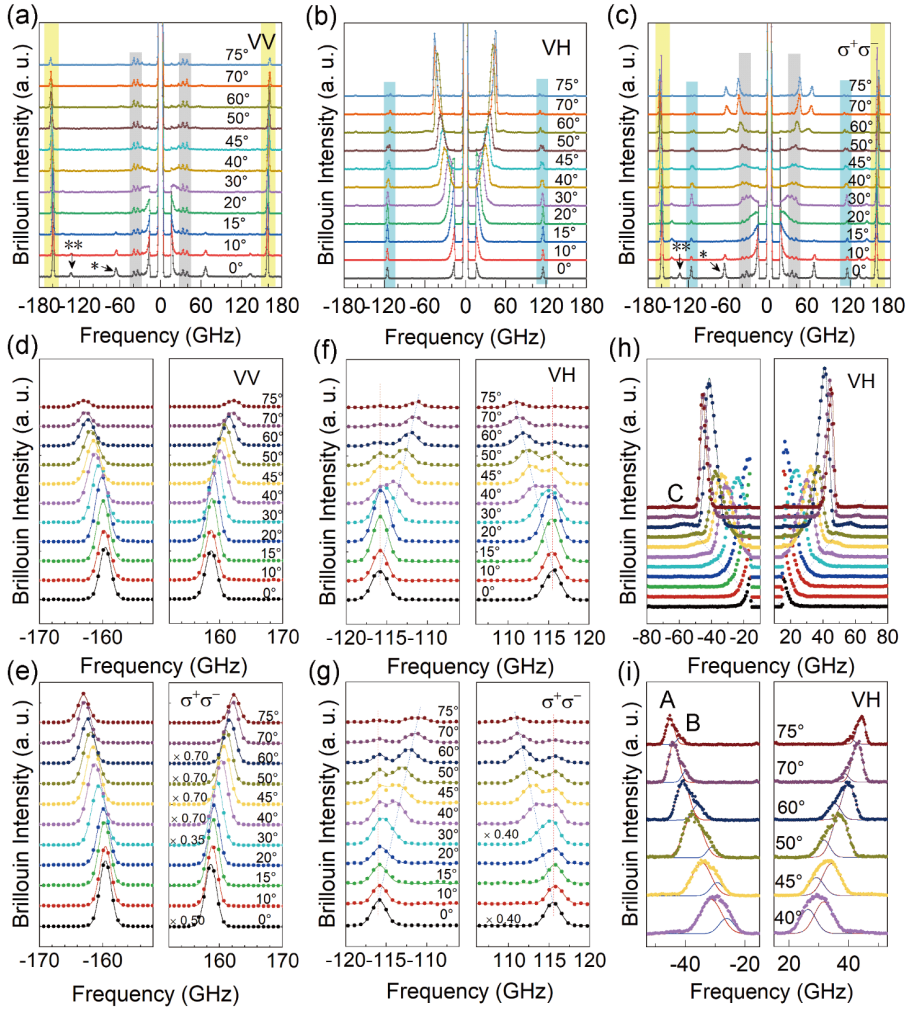

Figure 2 (Color online) Angle-resolved BLS spectra of diamond. (a)-(c) The angle-resolved BLS spectra of diamond under three polarization configurations. (a) VV; (b) VH; (c) $\sigma^+\sigma^-$. The LA mode shown by the yellow background and the TA mode is marked with the cyan background. The peaks marked with **, * and the two small sharp peaks with the gray background (frequency between 30-40 GHz) are spurious signals independent of samples. The frequency changes of (d), (e) LA mode, (f), (g) TA mode and (h) the RSAW (B) and two SSBWs (A and C) with the incident angle θ_i. Here we only mark the C mode in (h) and show spectra of A and B modes in (i) measured at higher resolution. The solid circles represent the experimental data. The solid lines represent the Gaussian fitting curves. The dashed lines in (f) and (g) are guides for the eyes.

phonons $\mathbf{q}_{\Gamma A}$ is a linear combination of $\mathbf{q}_{\Gamma X}$ and $\mathbf{q}_{\Gamma K}$, and $\mathbf{v}_{\Gamma A}$ is the vector sum of $\mathbf{v}_{\Gamma X}$ and $\mathbf{v}_{\Gamma K}$. Table 1 lists the velocities of the TA and LA modes along the Γ-A direction. In a parallelogram ACΓD with a 45° angle, we can easily find that:

$$\mathbf{v}_{\Gamma A}=\mathbf{v}_{\Gamma X}\frac{\mathbf{q}_{\Gamma X}}{\mathbf{q}}\cos\theta'_{\mathrm{i}}+\mathbf{v}_{\Gamma K}\frac{\mathbf{q}_{\Gamma K}}{\mathbf{q}}\cos(45^\circ-\theta'_{\mathrm{i}}), \tag{5}$$

where $\mathbf{q}_{\Gamma X}$ and $\mathbf{q}_{\Gamma K}$ are two components of $\mathbf{q}$ propagating along the Γ-X and Γ-K directions, while $\mathbf{v}_{\Gamma X}$ and $\mathbf{v}_{\Gamma K}$ are the velocities along the Γ-X and Γ-K axes, respectively. It is more important to obtain the velocities using the incident angle rather than the refractive angle:

$$\mathbf{v}_{\Gamma A}=\mathbf{v}_{\Gamma X}\frac{\sqrt{n^2-n_0^2\sin^2\theta_{\mathrm{i}}}}{n^2}\left(\sqrt{n^2-n_0^2\sin^2\theta_{\mathrm{i}}}-n_0\sin\theta_{\mathrm{i}}\right)$$
$$+\mathbf{v}_{\Gamma K}\frac{n_0\sin\theta_{\mathrm{i}}}{n^2}\left(\sqrt{n^2-n_0^2\sin^2\theta_{\mathrm{i}}}+n_0\sin\theta_{\mathrm{i}}\right), \tag{6}$$

where n_0=1 is the refractive index of air, θ_{i} is the incident angle between 0° and 90°, and the direction of diamond rotation around the z-axis cannot affect the sign of $\mathbf{v}_{\Gamma A}$. When θ_{i}=90°, θ'_{i} has a maximum θ'_{i}=24.3° based on Snell's law. Thus, we cannot measure the real LA and TA modes traveling along the Γ-K direction. By establishing the connection between the high-symmetry axes in the BZ and an arbitrary direction in the crystal, eq. (6) provides a convenient method to calculate the velocity of BAWs propagating along an arbitrary direction. Note that the existence of Γ-W phonons cannot be totally excluded if their velocity has significant differences from $v_{\Gamma K}$. This effect will lead $v_{\Gamma K}$ in eq. (6) to change with θ_{i} and we can approximately write $v_{\Gamma K}$ as $\mathbf{v}_{\Gamma K}=\mathbf{v}_0+\alpha\sin\theta_{\mathrm{i}}$. Here, $\mathbf{v}_0$ is the value of $v_{\Gamma K}$ determined at θ_{i}=0 and α is the θ_{i}-dependent coefficient of $v_{\Gamma K}$ when θ_{i} increases from 0° to 90° because of the contribution from the ΓW phonon. As θ_{i} increases, the value of $\mathbf{v}_0+\alpha\sin\theta_{\mathrm{i}}$ will be close to actual sound velocity along the ΓK direction.

In Figure 3(c), we fitted the velocity data of three BAWs with the revised eq. (6). Parameters are obtained by fitting: for the LA mode, $v_{\Gamma X}^{\mathrm{L}}$=1.744×10^6 cm/s and $v_{\Gamma K}^{\mathrm{L}}$ = (1.757+0.065sinθ_{i})×10^6 cm/s; for the TA$_1$ mode, $v_{\Gamma X}^{\mathrm{T}}=v_{\Gamma K}^{\mathrm{T}}$ = 1.268×10^6 cm/s; for the TA$_2$ mode, $v_{\Gamma X}^{\mathrm{T}}$=1.268×10^6 cm/s and $v_{\Gamma K}^{\mathrm{T}}$ = (1.173+3.46×10^{-5}sinθ_{i})×10^6 cm/s. The $v_{\Gamma K}$ of the LA mode is much more sensitive to the Γ-W phonon than that of the TA$_2$ mode. When θ_{i}=90°, $v_{\Gamma K}^{\mathrm{L}}$=1.822×10^6 cm/s and $v_{\Gamma K}^{\mathrm{T}}$= 1.173×10^6 cm/s, almost coinciding with previous reports. When $f=\pm5.73\times10^5 v$, we fitted frequency data of the three modes in Figure 3(d) and obtained the same conclusion, i.e., the velocity of the LA (TA) mode propagating along an arbitrary direction can be calculated with the vector sum method in IWs. In our experiments, the propagating direction of BAWs gradually changed from the Γ-X to Γ-K direction as θ_{i} increases. As shown in Table 1, for the LA mode, $v_{\Gamma X}<v_{\Gamma K}$; however, for the TA mode, $v_{\Gamma K}$ has two different values for two orthogonal vibration directions—one is equal to $v_{\Gamma X}$ and the other is smaller. Therefore, the LA peak is blueshift, the TA peak is split, and one of the TA peaks is redshifted during the rotation of the diamond sample.

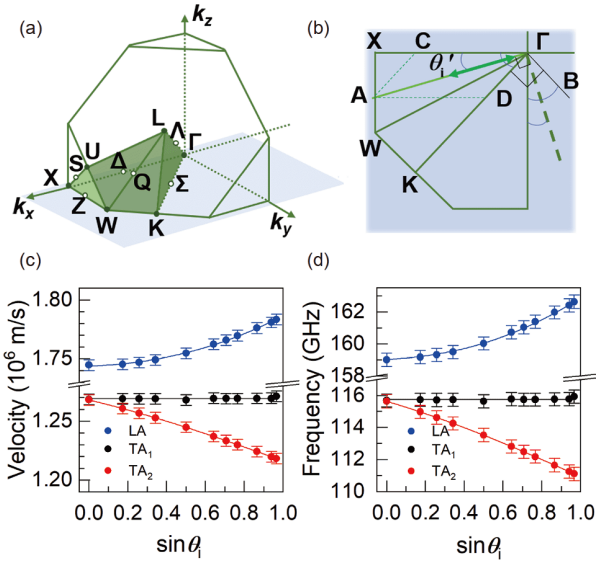

Figure 3 (Color online) Schematic diagrams of (a) the 1/8 of the first BZ and (b) the x-o-y plane of the first BZ. θ'_{i} corresponds to the refraction angle in real space. The green double-arrow indicates the wave vector of BAW. The dotted line is the auxiliary line for vector synthesis. (c) Velocity and (d) frequency of the BAWs of diamond as a function of sinθ_{i}. The solid circles represent experimental data. The solid lines are fitting curves based on (c) eq. (6) and (d) f=qv.

In contrast to BAWs, SAWs are typical acoustic modes propagating along the surface. SAWs can be observed only when $\mathbf{k}_{\mathrm{i}}$ has a projection on the surface, i.e., $\mathbf{q}^{\parallel}$ is non-zero. Under the angle-resolved BLS configuration, $\mathbf{q}^{\parallel}$ gradually increases as the angle θ_{i} increases. We reported that A, B, and C modes have the characteristics of SAW: their frequencies are almost 0 when θ_{i} = 0 and are obviously proportional to sinθ_{i}, as shown in Figure 4(b). Entropy fluctuation is a possible reason for the widening of Rayleigh lines at low angles [33]; however, it cannot explain the splitting of Rayleigh lines and the blueshift of these modes. As mentioned above, the SAW peaks are broadened because of the finite numerical aperture of the objective lens and the entrance aperture of the interferometer under a small θ_{i}. We use the above dispersion relationship of SAWs to linearly fit the experimental data of these three modes and obtain their velocities: v_{A}=(1.277±0.011)×10^6 cm/s, v_{B}=(1.080±0.009)×10^6 cm/s, and v_{C}=(1.727±0.010)×10^6 cm/s.

The B velocity mode meets the conditions of RSAW, which possesses a phase velocity of ~10% lower than that of the slower BAW (TA$_2$ in this work) on the same substrate surface. RSAW is primarily caused by coupling of longitudinal (L-) and shear vertical (SV-) type BAWs close to the surface; therefore, most of the energy is concentrated close to the surface [7], as schematically shown in Figure 4(a). Jiang et al. [34] reported that the calculated velocity of RSAW is

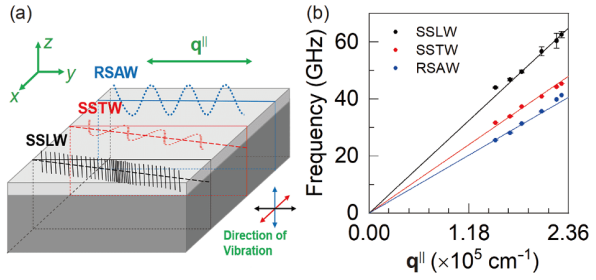

Figure 4 (Color online) Schematic diagrams (a) and the $f(\mathbf{q}^{\parallel})$ relation of RSAW and two SSBWs (b). (a) The area close to the surface is light gray, and the area far from the surface is dark gray. The propagating direction of each mode is parallel to the plane and shown in the same colors in (a) and (b). $\mathbf{q}^{\parallel}$ is the projection of the incident light wave vector on the surface. (b) The solid circles represent experimental data and the solid lines are fitting curves based on $f=\pm 2.36\times 10^5 \sin\theta_i v$.

10753 and the measured value is (10326±470) m/s using stimulated Brillouin scattering on polycrystalline CVD diamond film. Djemia et al. [35] reported that RSAW is (10800±300) m/s measured by BLS. Our result of $v_B=(1.080\pm 0.009)\times 10^6$ cm/s is consistent with their results; therefore, we attribute the B mode to the RSAW.

Notably, the velocity of SAW should be smaller than the slower TA mode [7], but the velocities of A and C modes are close to those of the TA and LA modes, respectively. Therefore, we can safely conclude that A and C modes are not SAWs. According to $n=f_{BAW}/f_{SAW}\sin\theta_i$, we calculate the refractive index $n_{LA}=2.483$ and $n_{TA}=2.419$, respectively, under $\theta_i=60°$. These values are consistent with the two high-speed SAW-like modes reported by Motochi et al. [27]. Here, we attribute A and C modes to shallow BAWs, which are called pseudo-SAWs [36] or surface skimming bulk waves (SSBWs) [7] in different applications. SSBWs originate from the components of BAWs propagating along the surface; however, their energy gradually leaks into the bulk at a propagation angle (the angle between the surface and the propagation direction) smaller than that of the leaky wave [37]. SSBWs are divided into surface skimming transverse waves (SSTWs) and surface skimming longitudinal waves (SSLWs) as per the different vibration directions. There are multiple SSBWs with different velocities in a plate-shaped material, and their velocities are related to the thickness of the plate and the thickness of the dielectric layer on the plate [36]. Here, our SSBWs could be from the interface between air and diamond layers. Because incident light is focused on the diamond surface, the velocity of SSBWs should be between that of the TA mode and LA mode. The velocities of A and C modes in our work are almost the same as the velocities of the TA mode and LA mode of diamond, respectively. Moreover, as shown in Figure 2(a) and (b), the polarization property of A mode is similar to the TA mode. Thus, the A mode is attributed to SSTWs, for which the vibration direction of particles (VDP) is parallel to the surface of the sample but perpendicular to the propagation direction of waves; the C mode is attributed to SSLWs [38], where the VDP is parallel to both the sample surface and the propagation direction of the wave, as shown in Figure 4(a). The propagation of SSBWs on substrates cannot be affected by surface roughness, and SSBWs have been applied to fabricate high-frequency and temperature-stable devices due to their high propagation velocity [39-41].

4 Conclusions

In this study, we examined acoustic velocities propagating along an arbitrary direction within a crystalline diamond with angle-resolved BLS spectroscopy. We determined the acoustic velocities of arbitrary BAWs as functions of the incident angle and the acoustic velocities of BAWs along the high-symmetry axis. As per the angle-resolved BLS spectra, we successfully identified three waves with SAW properties in the (100) face and discussed their physical mechanisms. Because SSBWs have a higher propagation velocity than RSAW, our results provide guidance for designing diamond-based surface acoustic devices with higher frequencies.

This work was supported by the National Basic Research Program of China (Grant Nos. 2016YFA0300804, and 2016YFA0301200), the Beijing Natural Science Foundation (Grant No. JQ18014), and the National Natural Science Foundation of China (Grant Nos. 12074371, and 51527901).

1 S. Mishra, and R. Bray, Phys. Rev. Lett. **39**, 222 (1977).
2 A. B. Singaraju, D. Bahl, and L. L. Stevens, AAPS Pharmscitech. **20**, 109 (2019).
3 K. S. Olsson, K. An, and X. Li, J. Phys. D-Appl. Phys. **51**, 133001 (2018).
4 B. Liu, X. Chen, H. L. Cai, M. A. Mohammad, X. G. Tian, L. Q. Tao, Y. Yang, and T. L. Ren, J. Semicond. **37**, 021001 (2016).
5 M. Knapp, R. Hoffmann, V. Lebedev, V. Cimalla, and O. Ambacher, Nanotechnology **29**, 105302 (2018).
6 R. Aigner, and G. Fattinger, in *2019 20th International Conference on Solid-State Sensors, Actuators and Microsystems & Eurosensors XXXIII* (Transducers & Eurosensors XXXIII, Berlin, 2019), pp. 523-526.
7 K. Hashimoto, *Surface Acoustic Wave Devices in Telecommunications: Modelling and Simulation* (Springer, Berlin, Heidelberg, 2000), pp. 1-23.
8 S. Evangelou, Phys. Lett. A **381**, 1624 (2017).
9 S. Yadav, A. Pamnani, D. Sharma, A. Gedam, A. Kumar, and N. Sharma, J. Semicond. **40**, 052901 (2019).
10 S. Zhang, R. Lu, H. Zhou, S. Link, Y. Yang, Z. Li, K. Huang, X. Ou, and S. Gong, IEEE Trans. Microwave Theor. Tech. **68**, 3653 (2020).
11 V. Mortet, O. Williams, and K. Haenen, in *Diamond-based acoustic devices*: *Physics and Applications of CVD Diamond*, edited by S. Koizumi, C. Nebel, and M. Nesladek (Wiley-VCH, Weinheim, 2008), pp. 177-197.
12 L. Wang, S. Chen, J. Zhang, J. Zhou, C. Yang, Y. Chen, and H. Duan, Appl. Phys. Lett. **113**, 093503 (2018).
13 D. Mukherjee, F. J. Oliveira, R. F. Silva, J. F. Carreira, L. Rino, M. R. Correia, S. Z. Rotter, L. N. Alves, and J. C. Mendes, Phys. Status Solidi C **13**, 53 (2016).

14 S. I. Burkov, O. P. Zolotova, B. P. Sorokin, P. P. Turchin, and V. S. Talismanov, J. Acoust. Soc. Am. **143**, 16 (2018).
15 R. Manenti, A. F. Kockum, A. Patterson, T. Behrle, J. Rahamim, G. Tancredi, F. Nori, and P. J. Leek, Nat. Commun. **8**, 975 (2017), arXiv: 1703.04495.
16 S. L. Ren, Q. H. Tan, and J. Zhang, J. Semicond. **40**, 071903 (2019).
17 S. Maity, L. Shao, S. Bogdanović, S. Meesala, Y. I. Sohn, N. Sinclair, B. Pingault, M. Chalupnik, C. Chia, L. Zheng, K. Lai, and M. Lončar, Nat. Commun. **11**, 193 (2020), arXiv: 1910.09710.
18 S. Meesala, Y. I. Sohn, B. Pingault, L. Shao, H. A. Atikian, J. Holzgrafe, M. Gündoğan, C. Stavrakas, A. Sipahigil, C. Chia, R. Evans, M. J. Burek, M. Zhang, L. Wu, J. L. Pacheco, J. Abraham, E. Bielejec, M. D. Lukin, M. Atatüre, and M. Lončar, Phys. Rev. B **97**, 205444 (2018), arXiv: 1801.09833.
19 D. Lee, K. W. Lee, J. V. Cady, P. Ovartchaiyapong, and A. C. Bleszynski Jayich, J. Opt. **19**, 033001 (2017), arXiv: 1609.00418.
20 D. A. Golter, T. Oo, M. Amezcua, K. A. Stewart, and H. Wang, Phys. Rev. Lett. **116**, 143602 (2016), arXiv: 1603.03804.
21 J. M. Lai, Y. R. Xie, and J. Zhang, Nano Res. **14**, 1711 (2021).
22 H. Sussner, J. Pelous, M. Schmidt, and R. Vacher, Solid State Commun. **36**, 123 (1980).
23 J. L. Warren, J. L. Yarnell, G. Dolling, and R. A. Cowley, Phys. Rev. **158**, 805 (1967).
24 B. Hammer, L. B. Hansen, and J. K. Nørskov, Phys. Rev. B **59**, 7413 (1999).
25 H. J. McSkimin, and P. Andreatch Jr., J. Appl. Phys. **43**, 2944 (1972).
26 M. H. Grimsditch, and A. K. Ramdas, Phys. Rev. B **11**, 3139 (1975).
27 I. Motochi, B. A. Mathe, S. R. Naidoo, and T. E. Derry, Mater. Today-Proc. **3**, S145 (2016).
28 L. Brillouin, Ann. Phys. **9**, 88 (1922).
29 L. I. Mandelstam, Z. Russ. Fiz-Khim. Ova. **58**, 381 (1926).
30 J. R. Sanderocock, Solid State Commun. **26**, 547 (1978).
31 P. K. Misra, *Physics of Condensed Matter* (Academic Press, London, 2012), pp. 1-35.
32 P. Y. Yu, and M. Cardona, *Fundamentals of Semiconductors* (Springer, Berlin, Heidelberg, 2003), pp. 17-106.
33 T. Wu, J. Shang, C. Yang, X. Zhang, H. Yu, Q. Mao, X. He, and Z. Chen, AIP Adv. **8**, 015210 (2018).
34 X. Jiang, J. V. Harzer, B. Hillebrands, C. Wild, and P. Koidl, Appl. Phys. Lett. **59**, 1055 (1991).
35 P. Djemia, C. Dugautier, T. Chauveau, E. Dogheche, M. I. De Barros, and L. Vandenbulcke, J. Appl. Phys. **90**, 3771 (2001).
36 E. Glushkov, N. Glushkova, and C. Zhang, J. Appl. Phys. **112**, 064911 (2012).
37 F. Monticone, and A. Alu, Proc. IEEE **103**, 793 (2015).
38 B. Köhler, M. Barth, P. Krüger, and F. Schubert, Appl. Phys. Lett. **101**, 074101 (2012).
39 A. A. Maradudin, and A. R. McGurn, Phys. Rev. B **39**, 8732 (1989).
40 J. S. Bach, and H. Bruus, Phys. Rev. E **100**, 023104 (2019), arXiv: 1905.09132.
41 K. H. Yen, K. F. Lau, and R. S. Kagiwada, Electron. Lett. **15**, 206 (1979).